TECHNICAL MEMORANDUM

799

Assimilation of Global Precipitation Mission (GPM) Microwave Imager (GMI) in all-sky conditions

Peter Lean, Alan Geer and Katrin Lonitz

Research Department

April 2017

European Centre for Medium-Range Weather Forecasts
Europäisches Zentrum für mittelfristige Wettervorhersage
Centre européen pour les prévisions météorologiques à moyen terme

Series: ECMWF Technical Memoranda

A full list of ECMWF Publications can be found on our web site under:
http://www.ecmwf.int/en/research/publications

Contact: library@ecmwf.int

Abstract

This memo describes the assimilation of the Global Precipitation Measurement (GPM) microwave imager (GMI) in all-sky conditions at ECMWF. GMI is a well-calibrated microwave imager that provides a good reference for evaluating the quality of simulated brightness temperatures. Biases between GMI observations and ECMWF simulations are all within the expected calibration uncertainty of 0.8 K, except in the 89 GHz channels. Previous microwave imagers have shown much larger biases (order 2 K to 4 K) so this is promising for the accuracy of the ECMWF model fields and observation operator, though more investigation is needed before final conclusions can be made. The assimilation of the GMI microwave imager channels in all-sky conditions was activated operationally in August 2015, and gives beneficial reductions in short and medium-range forecast errors of around 0.5%. Microwave imagers like GMI provide information on cloud and water vapour in the lower troposphere that is currently unique in the ECMWF analyses. The use of very long experiments has also given sufficient statistical power to confirm a small degradation of around 0.02% in the quality of dynamical forecasts in the lower-stratosphere, which further highlights a link between stratospheric dynamics and the assimilation of cloud and precipitation in the troposphere, most likely through tropical waves, although background error correlations cannot yet be ruled out. GMI also has humidity sounding channels, sensitive to the mid-troposphere. These will be activated in Cycle 43r3 in mid 2017, and their impact is beneficial but small, partly due to the great quantity of such data that is already being assimilated from sensors such as MHS.

1 Introduction

Since 2009, ECMWF has assimilated microwave imager radiances in all-sky conditions over ocean, taking data from up to three satellites simultaneously. All-sky microwave imager observations bring unique information on water vapour, cloud and precipitation, particularly in the lowermost troposphere, and provide around 4% of short-range forecast impact from the global observing system (measured by FSOI, Geer et al., 2017). This memo describes the implementation of the GMI instrument (Draper et al., 2015) which flies on the Global Precipitation Measurement (GPM) satellite, a joint mission between NASA and JAXA (National Aeronautics and Space Administration; Japan Aerospace Exploration Agency) that was launched in February 2014. GMI continues the heritage of the earlier TRMM microwave imager (TMI, Kummerow et al., 1998; Wentz et al., 2001) which was lost in April 2015. GMI can broadly be considered as TMI's replacement in the ECMWF assimilation system, since both imagers were designed to fly in a non-sun-synchronous orbit to provide information on the diurnal cycle of cloud and precipitation. However, GMI brings a number of interesting new capabilities. It has broader latitudinal coverage than TMI, good absolute calibration, and additional high frequency channels providing information on mid-tropospheric humidity and frozen hydrometeors.

2 Method

2.1 GMI instrument

2.1.1 Description

GMI (Draper et al., 2015) is a conical microwave imager using a spinning antenna of 1.22 m diameter to reflect passive microwave emissions from the earth into the instrument's feedhorns. Unlike cross-track scanning microwave sounders such as ATMS, this type of instrument observes the earth at a fixed zenith
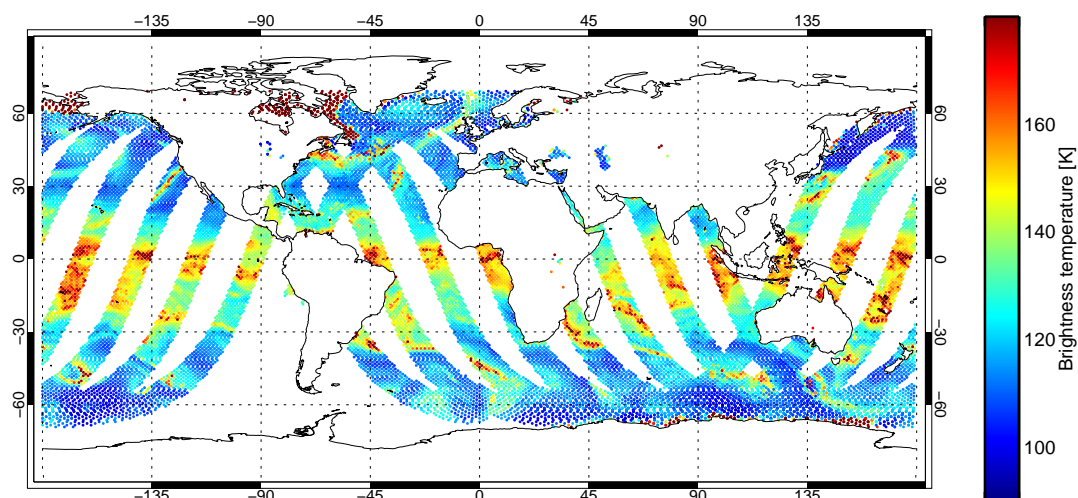
Figure 1: Coverage of GMI during a 12 h assimilation cycle from 21 UTC on March 10th to 09 UTC on March 11th, 2016. Observations have been screened to remove land surfaces and superobbed within an approximately 60 km radius. The colour scale shows the channel 10h observed brightness temperature.

angle, with fixed polarisation. The GPM satellite has a non-sun synchronous orbit with an inclination of 65°, meaning that it observes the tropics and midlatitudes, but not the polar regions (see Fig. 1).

One limitation of GMI compared to other microwave imagers is the swath width, which is 931 km for the GMI low-frequency channels, compared to for example 1450 km on AMSR2. This is because GPM also carries an active instrument, the Dual Polarisation Radar (DPR) which needs to operate from a relatively low altitude to minimise power requirements, and this necessarily implies a narrower swath for the conical scanning GMI. This lower operating altitude also helps give GPM's instruments a relatively high ground resolution. These are sensible design choices for a precipitation mission, but as will be seen they can reduce the impact in medium-range forecasting compared to similar instruments with a broader swath. For the moment the high spatial resolution is not important for global forecasting, since we superob the raw fields of view (see Sec. 2.2.3).

Table 1 shows the available channels. The first 9 channels approximately replicate the earlier TRMM microwave imager (TMI, Kummerow et al., 1998; Wentz et al., 2001) and are a standard microwave imager channel set, giving sensitivity to total column water vapour, precipitation, cloud water and frozen hydrometeors, as well as to the ocean surface. The higher frequency channels at 166 GHz and 183 GHz are new compared to TMI, and bring more information on cloud water, frozen hydrometeors, and the atmospheric moisture profile. The 183 GHz channels are humidity sounding channels similar to those on ATMS, MHS, SSMIS; however, there is no upper-tropospheric channel on GMI (no 183±1 GHz channel). The 166 GHz channels replicate the cloud-screening channels of these microwave humidity sounders, but the dual-polarisation capability is new, and for example is being used to investigate scattering effects from oriented cloud ice particles (Gong and Wu, 2017).

There is an important distinction between the GMI imager channels (1-9) and sounding channels (10-13), in that they observe at slightly different zenith angles (see Tab. 1) meaning that the observations are not colocated on the ground. At level 1B and 1C, the data come in two separate data streams (known as 'swaths') and essentially, the imager and sounder channels operate as independent instruments. A level

Table 1: GMI channels

Channel	Abbreviated name	Frequency [GHz]	Polarisation	Approx. zenith angle [degrees]	ECMWF use
1	10v	10.65	v	52.8	passive
2	10h	10.65	h	52.8	passive
3	19v	18.7	v	52.8	active (Aug. 2015)
4	19h	18.7	h	52.8	active (Aug. 2015)
5	24v	23.8	v	52.8	active (Aug. 2015)
6	37v	36.64	v	52.8	active (Aug. 2015)
7	37h	36.64	h	52.8	passive
8	89v	89	v	52.8	active (Aug. 2015)
9	89h	89	h	52.8	passive
10	166v	166	v	49.1	passive
11	166h	166	h	49.1	passive
12	183±3	183.31±3	v	49.1	active (Cy43r3, 2017)
13	183±7	183.31±7	v	49.1	active (Cy43r3, 2017)

1C-R product has become available, which colocates all the different channels to the same location, but since at ECMWF we superob the observations before assimilation, it is natural to use the superobbing process to colocate the data (Sec. 2.2.3).

ECMWF chose to assimilate the level 1C radiance product. Compared to level 1B, this applies inter-calibrations that are intended to bring the whole constellation of microwave imagers and sounders onto a common standard. Originally, the calibration standard was TMI, but since 3rd March 2016 (with the move of NASA processing version from V03 to V04) the intercalibration has been referenced to GMI level 1B. Hence, there should be no calibration difference between GMI 1B and 1C radiances after this date.

One issue with using level 1C radiances was that the change in calibration was not well communicated in advance, so at ECMWF we did not implement a precautionary blacklisting. Instead, the radiances continued to be assimilated operationally. The VarBC bias corrections were able to adapt to the new calibration within a single minimisation, but the problem was that for the analysis of 00Z 3rd March, we assimilated a mix of data, some with the old calibration and some with the new, with a bias correction that attempted to find a balance somewhere between the two. Figure 2 shows the VarBC transition for channel 19v taking two cycles, and the intermediate cycle (00Z 3rd March) has a bias correction that is about half-way between, because of the mix of old and new data. There was also a small longer-term spinup of around a week as a new balance was found between the constant term and others (skin temperature, surface wind speed and total column water vapour - these bias corrections will be examined in more detail in the next section). The analysis of 00Z 3rd does not seem to have been badly affected as there is no sign of a spike in the analysis standard deviation with respect to other all-sky microwave imagers, such as SSMIS. Hence it is unlikely the incident had any negative impact on forecasts. Some of the data was rejected and other data was downweighted by VarQC. Hence, although undesirable, the incident does not seem to have caused major problems, and it enabled the current situation of minimal bias between GMI and ECMWF simulations, which is examined further in the next section.
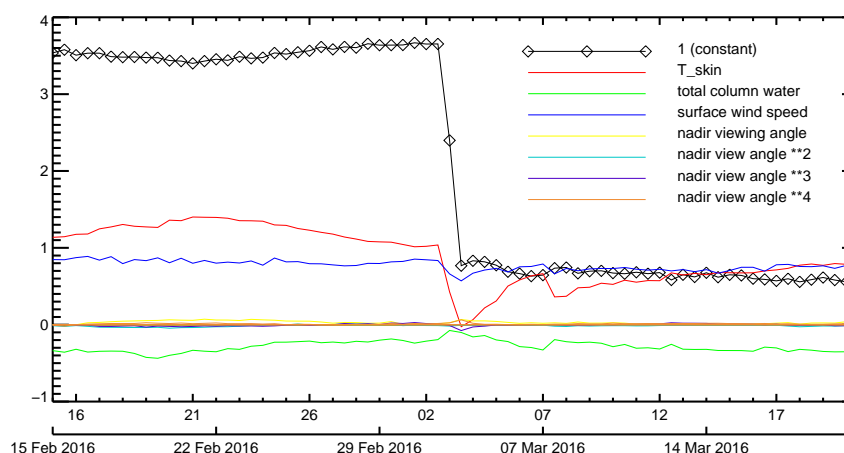
Figure 2: VarBC coefficient values, after analysis, for GMI channel 3 (19v) in operations during the transition of GMI 1C data from V03 to V04 calibration on 2nd March 2016 and also the transition from cycle 41r1 to cycle 41r2 on 8th March 2016. Similar results are seen in other channels. VarBC coefficient units are related to the predictors, but are also scaled, so there is no straightforward correspondence with brightness temperatures, except for the constant offset predictor, which can be interpreted as a brightness temperature bias in Kelvin.

2.1.2 Data quality and calibration

A big part of GMI's mission is to act as a transfer standard for intercalibration with other microwave imagers and sounders. Hence, special attention has been paid to ensuring accurate calibration, and to avoid issues that have affected past conical scanners, such as solar intrusions into the warm load calibration, or reflectors with imperfect reflectivity (e.g. Bell et al., 2008; Geer et al., 2010). For GMI, the warm load has been carefully protected against solar intrusion, and ground measurements of the reflector show a reflectivity of over 0.9999. The required maximum calibration uncertainty was 1.35 K for the imager channels, and in practice the instrument is thought to have achieved a calibration uncertainty of 0.8 K (Draper et al., 2015). Calibration stability is also thought to be within its 0.5 K requirement.

Figure 3a examines the biases of GMI and other microwave imagers using the ECMWF simulations as a reference standard. Note however that cloud-affected scenes have been removed: the ECMWF all-sky methodology will be introduced in more detail later, but broadly these statistics are computed using superobbed observations and a symmetric cloud screening to eliminate optically thicker cloud and precipitation where it affects either the observations or the FG. Biases between GMI and the ECMWF first guess are within the expected 0.8 K for all channels except 89v and 89h. The 89 GHz channels have great sensitivity to cloud water and water vapour, so it is possible that the bias of around 1.5 K could be explained by an ECMWF model bias, either in the model fields or in the observation operator. SSMIS is known to have calibration issues, so it is unsurprising to see much larger biases. AMSR2, as examined by Kazumori et al. (2016), is also thought to be a very stable, well calibrated instrument, so it is surprising to see systematic biases of between 2 K and 4 K relative to the ECMWF simulations and the GMI observations. These biases have become larger since the Kazumori et al. study, apparently due to the transition of the surface emissivity model at ECMWF from FASTEM-5 to FASTEM-6. However, this difference in calibration between AMSR2 and GMI is consistent with results from direct intercomparisons (Berg et al., 2016). Given that we use VarBC bias correction, it is not a major issue for the current assimilation system. Overall it seems the absolute calibration of GMI agrees very well with that of ECMWF simulations.
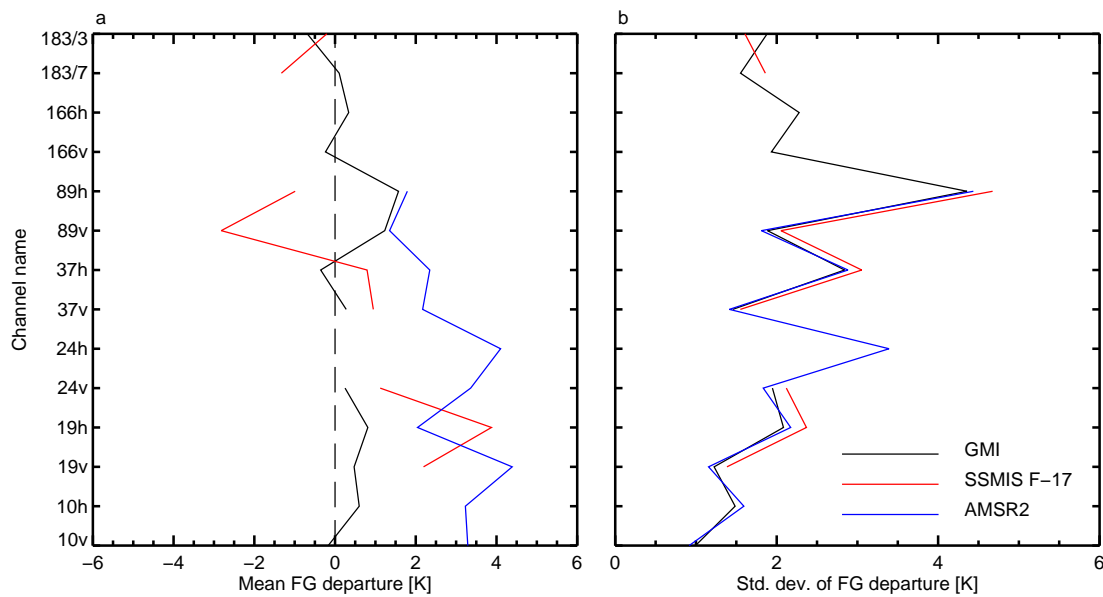
Figure 3: a) bias; b) standard deviation of GMI, SSMIS F-17 and AMSR2 FG departures. The bias has been computed before VarBC bias correction, focusing attention on the absolute calibration of the instruments; the standard deviation is that of bias-corrected FG departures, highlighting any problems of calibration stability that are not handled by the VarBC bias model. Observations have all been superobbed to the same spatial resolution in a circle of approximately 60 km radius, and any observations or first guess affected by significant cloud has been screened using a threshold on the normalised polarisation difference (see Geer and Bauer, 2010). The sample is from 21st – 30th August 2016 and as far as possible (this excludes the 183 GHz channels) a similar sample of data are chosen from each instrument. The screening that has been applied is largely independent of the usual IFS screening decisions (for example no background or VarQC checks have been applied) and instead observations have been eliminated only when it has not been possible to compute an accurate simulation, by excluding the following: land or coastal scenes, sea-ice, surface temperatures less than 274 K, cold-air outbreak regions, missing brightness temperatures (these occur at the GMI swath edge, where the high-frequency swath is not available), and negative moisture in the forecast model (a very rare failure).

Panel b of Fig. 3 examines the standard deviation of bias-corrected FG departures. Because of the superobbing (and the presence of forecast model errors) this is not a measure of the instrument noise (NEDT), but it can highlight any problems of calibration stability that are not handled by the VarBC bias model. Indeed, GMI and AMSR2 have very similar standard deviations, while those of F-17 SSMIS are slightly larger, likely a result of well-known solar-dependent biases that vary through the orbit. The figure shows results from a 10-day period, but long-term ECMWF monitoring (not shown) demonstrates GMI has had stable calibration for over a year since the March 2016 calibration change described previously. This suggests that GMI shows similar calibration stability to AMSR2 and better stability than SSMIS.

Despite the overall good agreement, a closer examination reveals remaining biases in the comparison between GMI and the ECMWF FG, of varying origin. Figure 4 panels a–d show the channel 19v bias correction, binned as a function of the predictors in the VarBC bias model for the same sample as before, i.e. mostly cloud-free scenes (see Fig. 2 for more details of the VarBC predictors). As a function of 10m windspeed, bias varies by 4 K (panel a). This is likely a real problem with the quality of surface emissivity modelling in the observation operator (the FASTEM-6 model Bormann et al., 2012; Kazumori and English, 2015). The bias is consistent with the results of Meunier et al. (2014), who showed it could be improved in the future by better representation of ocean foam coverage. However, the bias-corrected FG departures, also shown on the figure, have little residual bias, indicating that VarBC is working well. Biases also vary as a function of skin temperature and total column water vapour (TCWV, panels b and c) but in general, not by more than 1 K. It would be hard to attribute these biases but the forward modelling (i.e. the forecast model or observation operator) would be the most likely explanation; these biases are unlikely to be related to the GMI instrument. However, panel d shows the bias correction as a function of the GMI scan position. This ranges from 0.5 K to 0.7 K, indicating there is a residual cross-scan bias of order 0.2 K. The magnitude of cross-scan bias is no bigger than this in most channels, but it does reach O(0.5K) in 10v, 10h, 166v and 166h, and O(1K) in 183 GHz channels in scan positions above 210 (not shown). These cross-scan biases are most likely a real issue of the GMI instrument, though again they are largely within the calibration stability requirement of 0.5 K, mostly well corrected by VarBC, and relatively small compared to the observation errors used in the ECMWF system (next section, Figs. 6 and 7).

Finally, Fig. 4 panel e examines cloud-dependent bias using the recommended 'symmetric' cloud predictor of Geer and Bauer (2010) which takes an average of the 'cloud amount' estimated from simulated and observed brightness temperatures, to avoid sampling bias. The bias correction does not use this as a predictor, so as expected the bias correction is flat as a function of cloud amount. However, there is some residual bias left in the FG departures for symmetric cloud amounts of larger than 0.2. This is tolerated because this bias is small compared to the size of observation errors in cloudy conditions. For the majority of clear-sky observations, the bias is small.

Figure 5 shows the bias corrections at 89v, which are illustrative of the higher frequency channels. No significant windspeed-dependence is generated in the bias correction (panel a). In fact, the surface emissivity modelling problem is only seen at 37 GHz and below (not shown). As a function of skin temperature and TCWV, biases are larger, varying by up to 2 K. As mentioned before, there are likely systematic errors in the forecast model or observation operator that map onto these predictors: for the mostly-cloud-free sample, 89 GHz would be very sensitive to any TCWV biases in the modelling, but also to cloud liquid water below the arbitrary 'clear-sky' cutoff point. There are large and well-known biases in the ECMWF modelling of low-level liquid water cloud that would show up most clearly at 89 GHz (e.g. Kazumori et al., 2016; Lonitz and Geer, 2017). The scan-dependent bias is small in this channel (panel d). Including heavily cloudy and precipitating scenes in panel e confirms that cloud-dependent bias is large in this channel, but again mostly for the highest cloud amounts where it does not matter so much,
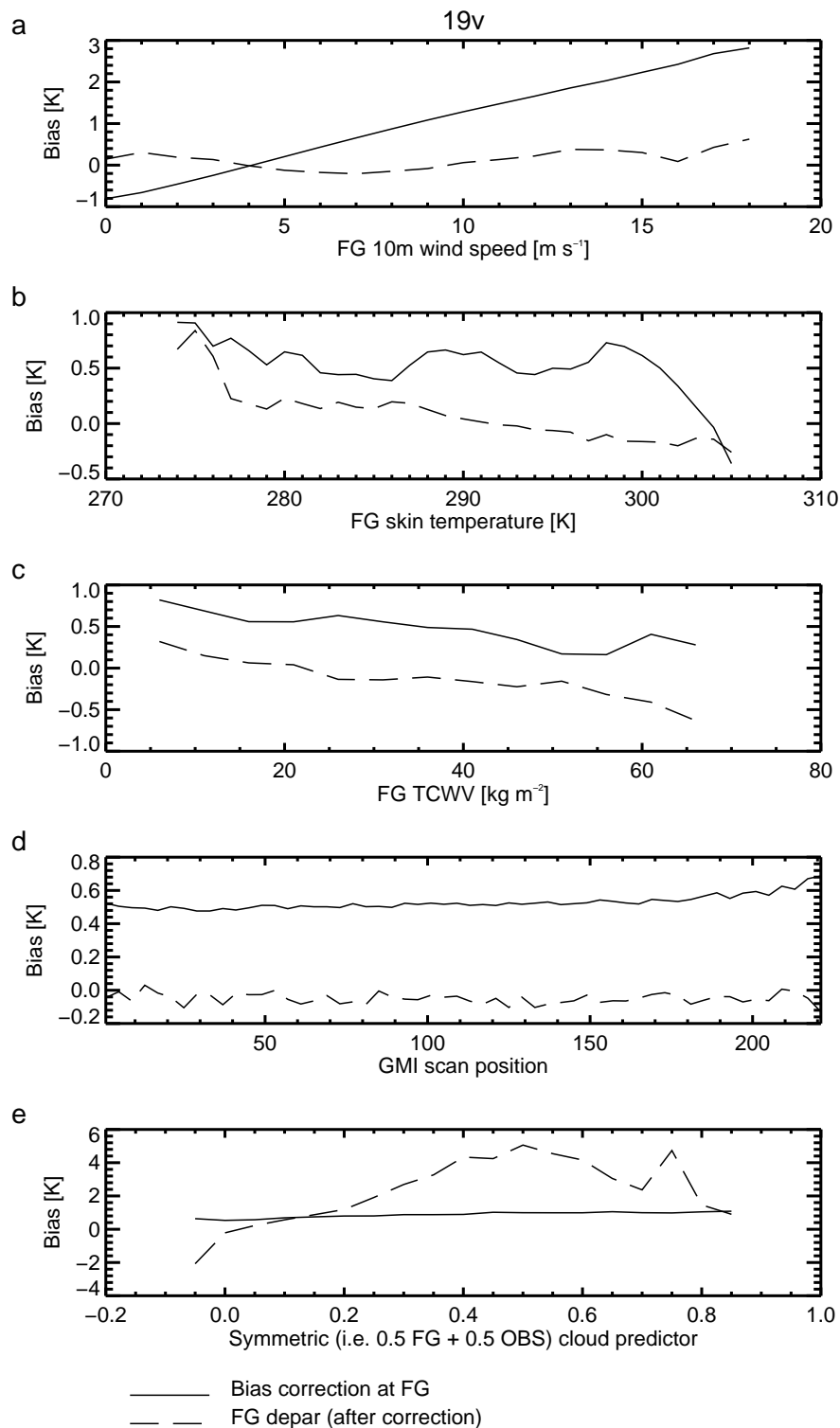
Figure 4: *Total VarBC bias correction (solid) and FG departure after bias correction (dashed) as a function of various predictors, for GMI channel 19v. The sample is the same as in Fig. 3 except for in panel e, where the cloud screening has been removed, so that cloudy and precipitating scenes are included.*

Figure 5: *Total VarBC bias correction (solid) and FG departure after bias correction (dashed) as a function of various predictors, for GMI channel 89v. The sample is the same as in Fig. 3 except for in panel e, where the cloud screening has been removed, so that cloudy and precipitating scenes are included.*
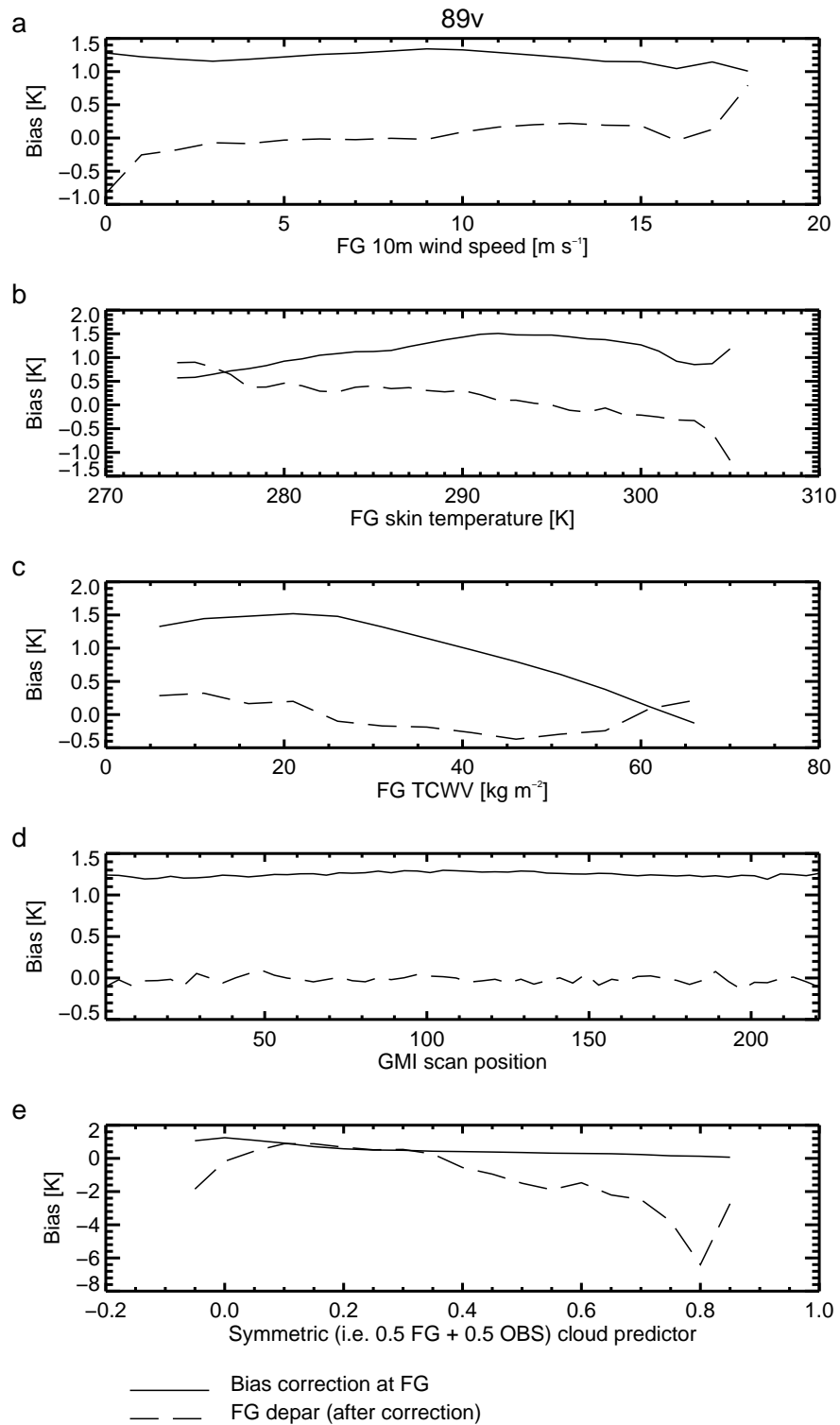
due to the size of observation errors.

To conclude, this section has shown that the calibration of the ECMWF FG and GMI are overall consistent, within GMI's expected calibration accuracy for most channels. The calibration stability is as good as that of AMSR2 and better than SSMIS. However, cross-scan biases of 0.2 K to 1 K remain. There are also a number of biases between ECMWF and GMI, most prominently those that are dependent on cloud amount and near-surface windspeed, which likely highlight systematic errors in the forecast model or the observation operator.

2.2 Implementation in the IFS

2.2.1 Overview

GMI has been implemented within ECMWF's all-sky assimilation stream, described in more detail by Bauer et al. (2010), Geer and Bauer (2010) and Geer et al. (2017). All observations, whether clear, cloud or precipitating, are expected to be assimilated, and the observation-equivalent is simulated using a scattering-capable radiative transfer model RTTOV-SCATT (Bauer et al., 2006), currently at RTTOV version 11.3. Observations are superobbed onto a common resolution that is intended to be representative of the spatial scales of the forecast model; this is a circle of approximately 60 km radius. Standard ECMWF quality control is applied including a check on the size of the normalised FG departures, and also variational quality control (VarQC, Järvinen and Unden, 1997). Specific all-sky quality checks are also applied, some of which are listed in the caption to Fig. 3; further details can be found in the cited literature. A VarBC bias correction (Dee, 2004) is also applied, as has been illustrated in Fig. 2; this figure also summarises the choice of VarBC predictors for the imager channels.

As is standard for microwave imaging channels at ECMWF, the data are only used over ocean, and within $60°$ of the equator, to avoid areas where surface emissivity modelling errors can become large. Table 1 summarises the imager channel usage; we do not yet assimilate 10 GHz channels, due to the difficulty of accurately simulating this frequency, which exposes systematic modelling errors in precipitation and surface emissivity. Also, since the start of direct all-sky assimilation of microwave imagers in 2009, the 37h and 89h channels have been excluded, in theory due to their larger sensitivity to cloud errors (this may not necessarily be true any more and future work should examine whether these channels can now be assimilated.)

The GMI microwave imager channels were activated in the ECMWF operational system in August 2015. The 183 GHz water vapour sounding channels were not initially activated, for technical reasons: because of a bug in pre-processing that scrambled the channel mapping (see later) and because the necessary work had not been done to allow multiple zenith angles ($52.8°$ for imager channels and $49.1°$ for sounder channels) in the same RTTOV simulation. These problems have since been solved and the 183 GHz channels will be activated in cycle 43r3. Usage is currently only over ice-free oceans, similar to that of the imager channels; future work would be needed to apply the same utilisation strategy as MHS and SSMIS, for which almost all surface types can be actively assimilated.

2.2.2 Observation errors

The observation error model of Geer and Bauer (2010, 2011) is applied to GMI, using the original symmetric predictor, which is based on normalised polarisation difference at 37 GHz. As is done for SSMIS, this predictor is used for modelling the 183 GHz channel errors over ocean, as well as for the
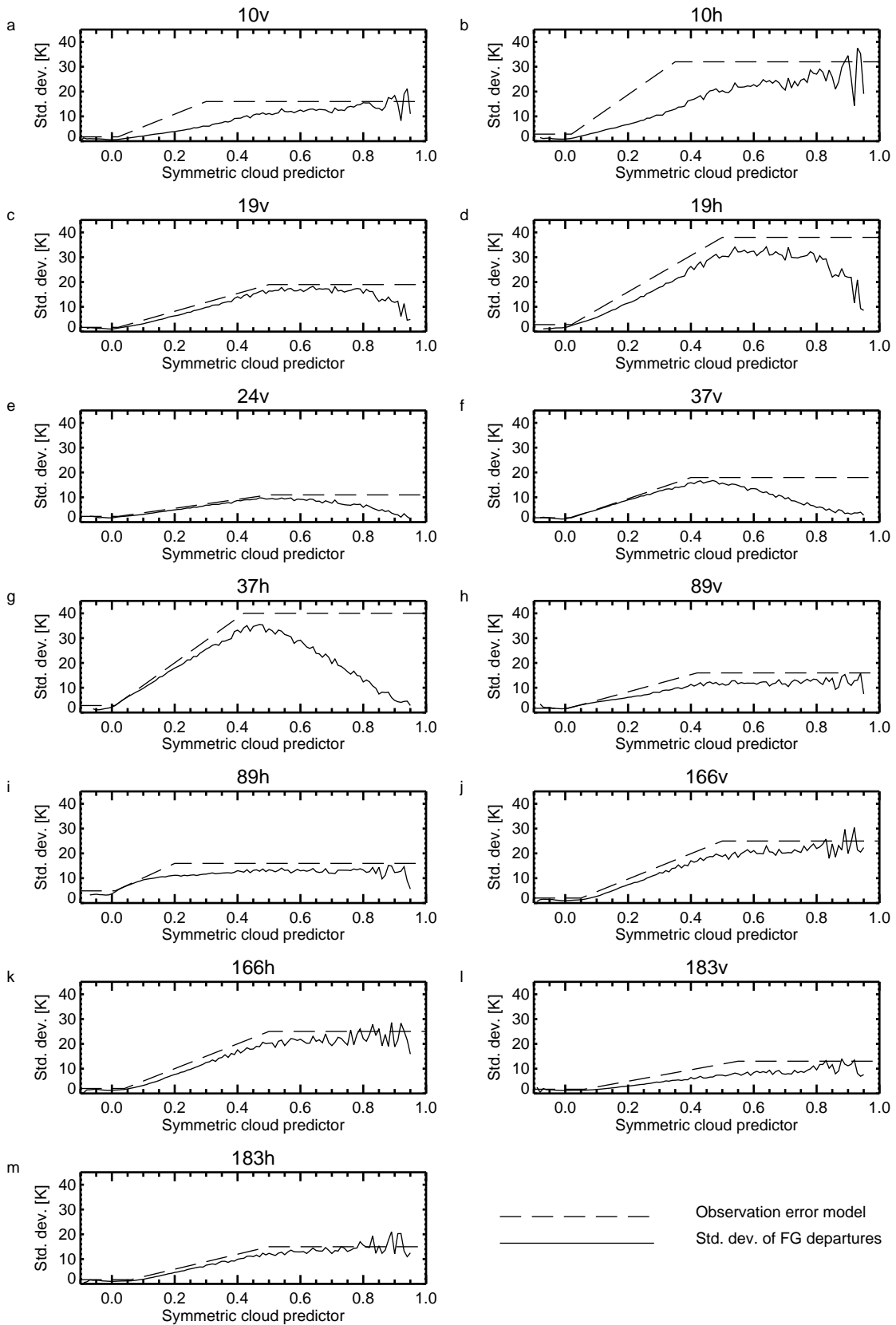
Figure 6: *Observation error model (dashed line) compared to standard deviation of FG departures (solid line) as a function of the symmetric cloud predictor. Bin size is 0.01.*
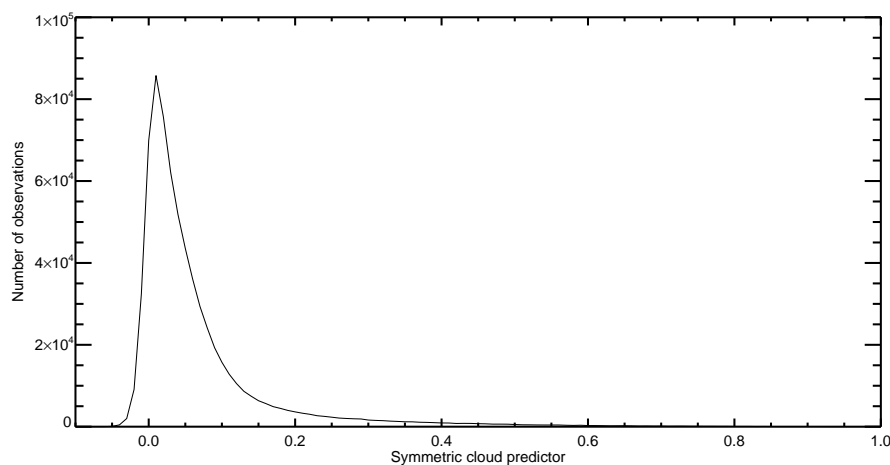
Figure 7: Number of observations as a function of the symmetric cloud predictor, for a set of screened, assimilated channel 37v observations (other channels show similar results). Bin size is 0.01.

imager channels. Figure 6 shows the observation error model as a function of this predictor, compared to the standard deviation of FG departures, which it is supposed to fit approximately. The sample of data used here is all active or passively monitored observations, depending on the channel. The modelled errors are a little larger than the standard deviation of FG departures. This is because the model was fitted closely to the FG departures of a sample of passively monitored observations before the instrument was active in the system. During passive monitoring, the usual FG departure check and VarQC cannot be applied as they only work correctly once an observation error model has been defined. This approach is normal practice for a new instrument and results in a slight over-estimate of observation errors; a more precise approach would require an iterative solution that has not yet been considered to be worth the additional effort.

Figure 7 shows an example of the number of observations falling in each bin, for the 37v channel. Negative values of cloud predictor are caused by the aliasing of FG humidity errors into the normalised 37 GHz polarisation difference, and are not a major problem.

2.2.3 Technical issues

As described earlier, data from the GMI imager channels (1-9) and sounding channels (10-13) come in two separate data streams and the individual fields of view within each swath are not exactly co-located. The GMI imager and sounder data are retrieved from MARS as independent data streams. Each stream undergoes BUFR pre-screening and superobbing onto a T255-equivalent reduced Gaussian model grid (and this has half the grid points removed in a diamond pattern, for additional thinning). Superobbing the imager and sounding channels to the same grid is a way of colocating them. Technically, for subsequent processing in IFS, it is desirable to have data from all of the channels combined into a single report in ODB. To achieve this, a new match-up process was written to combine co-located data from the two swaths during the bufr2odb processing stage. Consequently, ODB presents IFS with data from all 13 GMI channels combined together within each report.

A separate issue arose in the conversion of the NASA HDF format GMI raw data files to BUFR: the assignment of channels 10-13 to the observed radiances was initially incorrect. Compared to the correct channel mapping (Tab. 1) the radiances had been 'left rotated' by one, so for example channel 10 incor-

rectly contained 166h observations while channel 13 got the 166v observations. Note that channels 1-9, which were processed separately, were fine. The problem was corrected in the BUFR ingestion software in operational cycles starting 2nd November 2016. Earlier GMI data has now been reprocessed. The correction of this issue, along with the ability to handle multiple zenith angles in a single observation, finally allowed the high frequency channels to be considered for operational assimilation in cycle 43r3, due for implementation in mid 2017.

3 Results: imager channels

3.1 Details

This section summarises the results of experiments run prior to operational implementation in cycle 41r1 in August 2015. These experiments used the full-resolution operational configuration of the IFS, which was TL1279 at the time, and were subsequently extended into the months before and after to create a sample of scores for verification of around 13 months duration, covering 25th October 2014 to 1st December 2015. The control is identical to the operational system in May 2015, after TMI had been lost. Only one microwave imager was being assimilated in the system at that time: SSMIS F-17. A fixed blacklist is used to keep TMI switched off in the period when it would otherwise have been assimilated, and to ignore the operational implementation of GMI and AMSR2 in August 2015. What this means is that, for microwave imagers, the control has SSMIS active, and the experiment contains GMI and SSMIS active. This long experimental period gives a good chance to see significant forecast impact from GMI.

3.2 Forecast scores

Short-range impact is most reliably measured by observation fits. Figure 8 shows the humidity impact of GMI assimilation. Although IASI and ATMS have temperature sensitivities (in the case of ATMS, with consistent results to AMSU-A, see later) it is the humidity impact that stands out, reaching 0.5% to 0.3% in mid and upper-tropospheric channels (IASI channels 2500 – 3000; ATMS channels 18 – 22) and in tropospheric temperature channels with some humidity sensitivity, particularly to the lower troposphere (other IASI channels). Radiosondes also show a 0.3% improvement in the lower troposphere. Given that GMI's main information content is column water vapour and integrated cloud water, this makes sense. SSMIS channels 12 – 17 are microwave imager channels similar to those on GMI, and they show up to 2% reduction in FG departures, again suggesting improvements in lower-tropospheric moisture and cloud forecasts.

Figure 9 shows the impact of GMI assimilation on temperature observations. The radiosonde and satellite measurements are broadly in agreement over the 0.05% to 0.1% reduction in temperature FG departures between about 500 hPa and 850 hPa. This is also supported by aircraft observations (not shown) and indicates a real improvement in lower-tropospheric temperatures. This would be expected through the 4D-Var tracing mechanism (e.g Bauer et al., 2010; Geer et al., 2014) and is consistent with previous studies (e.g Kazumori et al., 2016).

The temperature fits also indicate issues in the stratosphere. AMSU-A shows an increase in FG departures of 0.02% in channels 11 and 12, which are sensitive roughly to between 20 km and 35 km altitude. These degradations are backed up by GPSRO (not shown) and can be localised to the tropics and SH. Similar issues have been seen in other AMSU-A stratospheric channels in previous microwave imager testing (e.g channel 9, Kazumori et al., 2016). This continues to build a picture of all-sky microwave
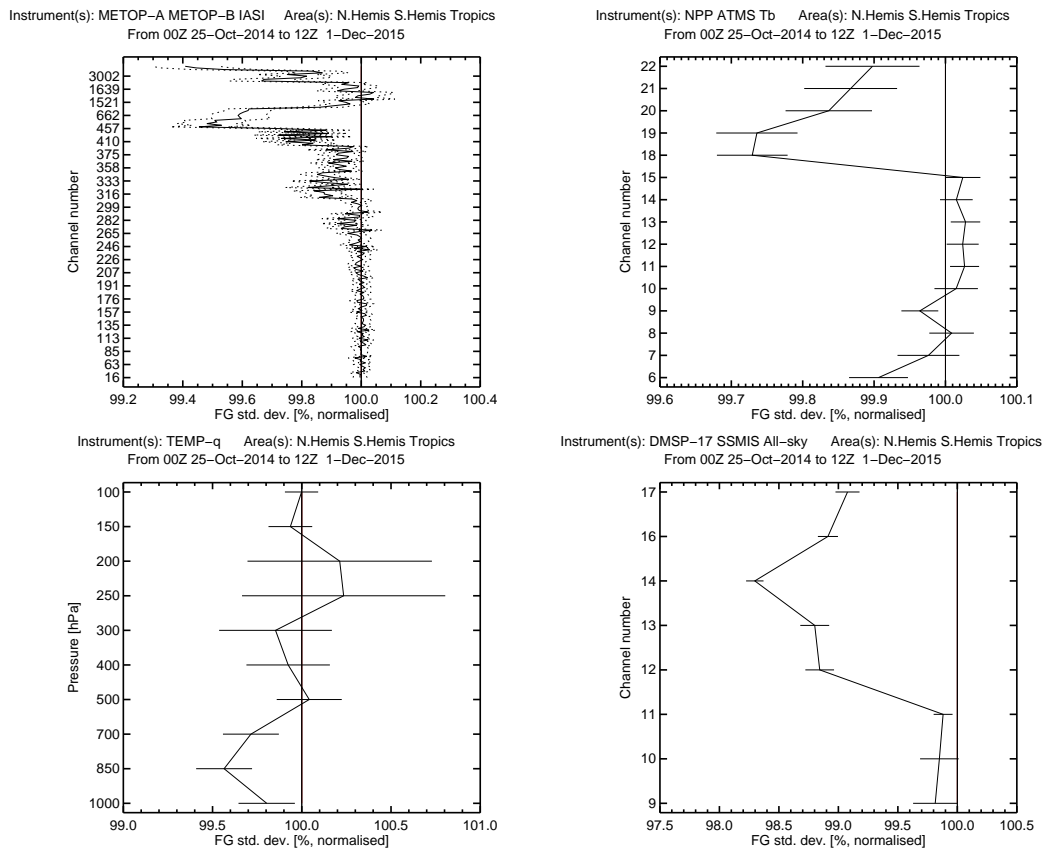
Figure 8: Normalised change in standard deviation of FG departures for observations with humidity sensitivity (and also temperature sensitivity; as a percentage of experiment divided by control): top left, IASI; top right, ATMS; bottom left, radiosonde TEMP-q; bottom right SSMIS
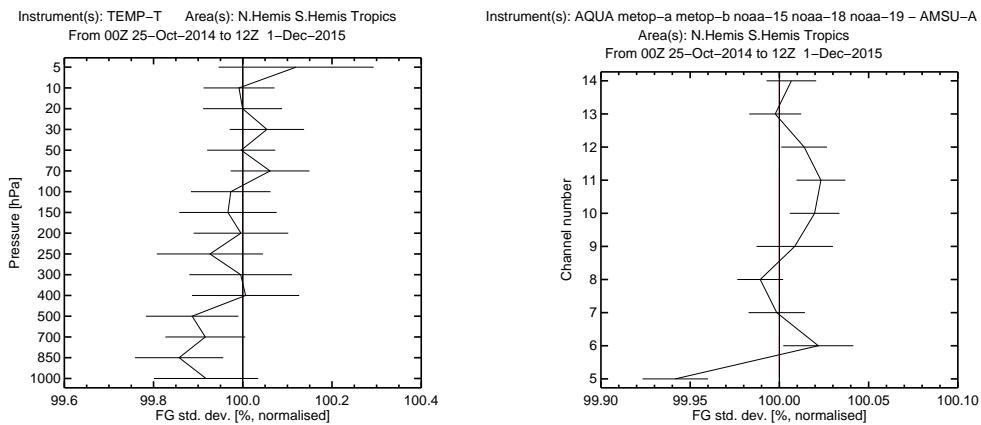

Figure 9: Normalised change in standard deviation of FG departures for temperature-related observations (as a percentage of experiment divided by control): left, radiosonde (TEMP-T); right, AMSU-A
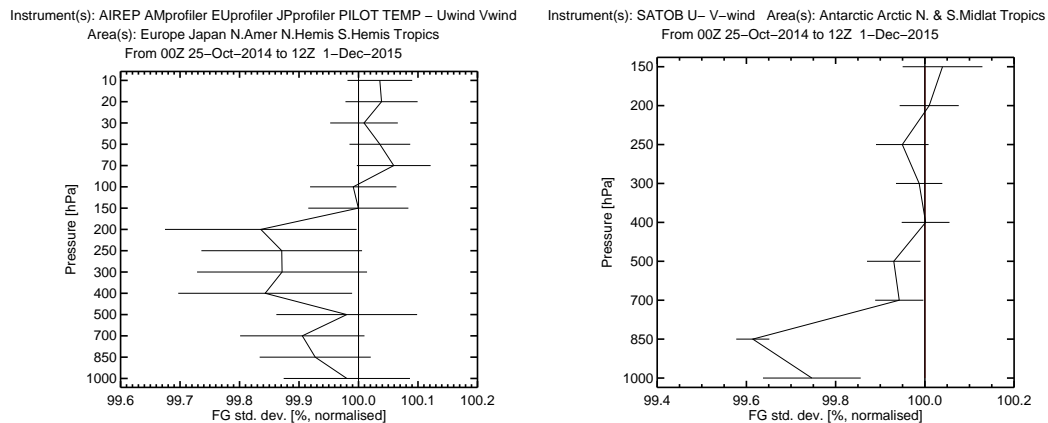
Figure 10: Normalised change in standard deviation of FG departures for wind observations (as a percentage of experiment divided by control): left, all conventional winds (WIND2); right, atmospheric motion vectors (SATOB)

imager assimilation having real but very slight negative impacts on FG temperature departures in the stratosphere, particularly in the tropics. Hypotheses to explain this could be (a) undesirable long-range correlations in the background errors, or (b) the activation or relocation of convection with subsequent propagation of gravity waves and other tropical waves into the stratosphere. The second possibility need not indicate a fundamental problem, and could just be seen as additional noise. Further, note that assimilation of all-sky humidity sounding channels is significantly beneficial to the stratosphere (e.g. Geer et al., 2014) possibly through similar mechanisms. In any case, the negative effect of microwave imagers is tiny and insignificant when compared to its other beneficial effects.

Figure 10 shows the wind impact of GMI, again expected through the 4D-var tracing effect and consistent with previous results for microwave imagers. Although the conventional wind impact is barely significant globally, these results actually smooth out some clearly significant benefits that are observed more locally: for example, U-winds improve by 0.2% in the NH at 300 hPa to 400 hPa; both wind components improve in the tropics around 700 – 850 hPa. Atmospheric motion vectors (AMVs, aka SATOBs) confirm similar impacts globally. The 4D-Var system is successfully using water vapour, cloud and precipitation from the GMI observations to infer winds.

Medium-range forecast impact is best measured with analysis-based scores. Significant impact from GMI can be seen in the NH at days 3-4, at around 0.6% magnitude (Fig. 11). The tests of Kazumori et al. (2016) showed that the addition of AMSR-2 or SSMIS to a system with no other microwave imagers would improve SH and NH medium-range scores by about 1%. Given that in the current testing GMI is being added into a system which already contains SSMIS, and given its smaller swath width, we would not expect to see quite so much impact.

To represent the zonal distribution of forecast impacts, Fig. 12 shows the change in vector wind error. As these results are based on own-analysis verification, the small increases in the short range probably come from increased wind increments, rather than from a real decrease in forecast quality. The observational verification of the 12 h forecast shows broad improvements in the wind field (see earlier.) Beyond the first day, the impact is largely to reduce wind forecast errors, although the statistical significance is low. Interestingly, past testing (Kazumori et al., 2016) showed microwave imager assimilation causing a larger increase in T+12 and T+24 'increments'. It is not clear if the reduction of this effect in the GMI results is significant or not.
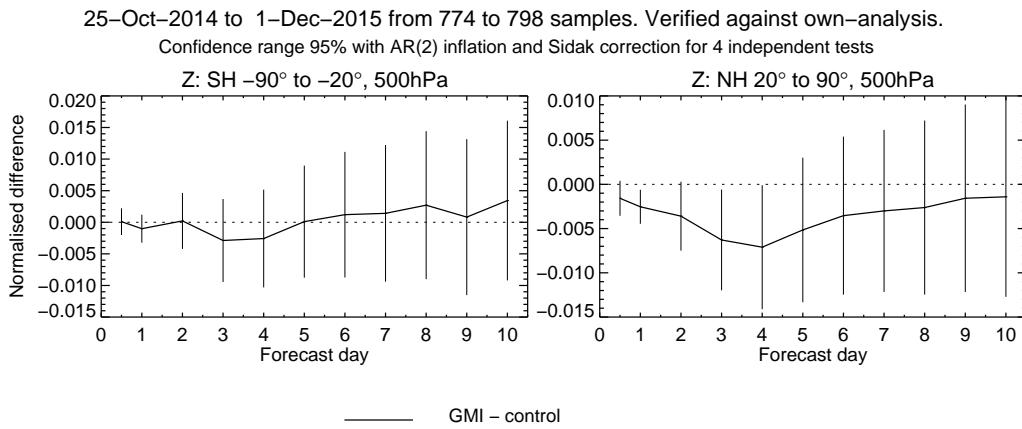
25–Oct–2014 to 1–Dec–2015 from 774 to 798 samples. Verified against own–analysis.
Confidence range 95% with AR(2) inflation and Sidak correction for 4 independent tests

Z: SH –90° to –20°, 500hPa

Z: NH 20° to 90°, 500hPa

GMI – control

Figure 11: Normalised change in RMS error in 500 hPa geopotential between GMI on and GMI off.

Change in error in VW (GMI–control)

25–Oct–2014 to 1–Dec–2015 from 774 to 798 samples. Cross–hatching indicates 95% confidence. Verified against own–analysis.
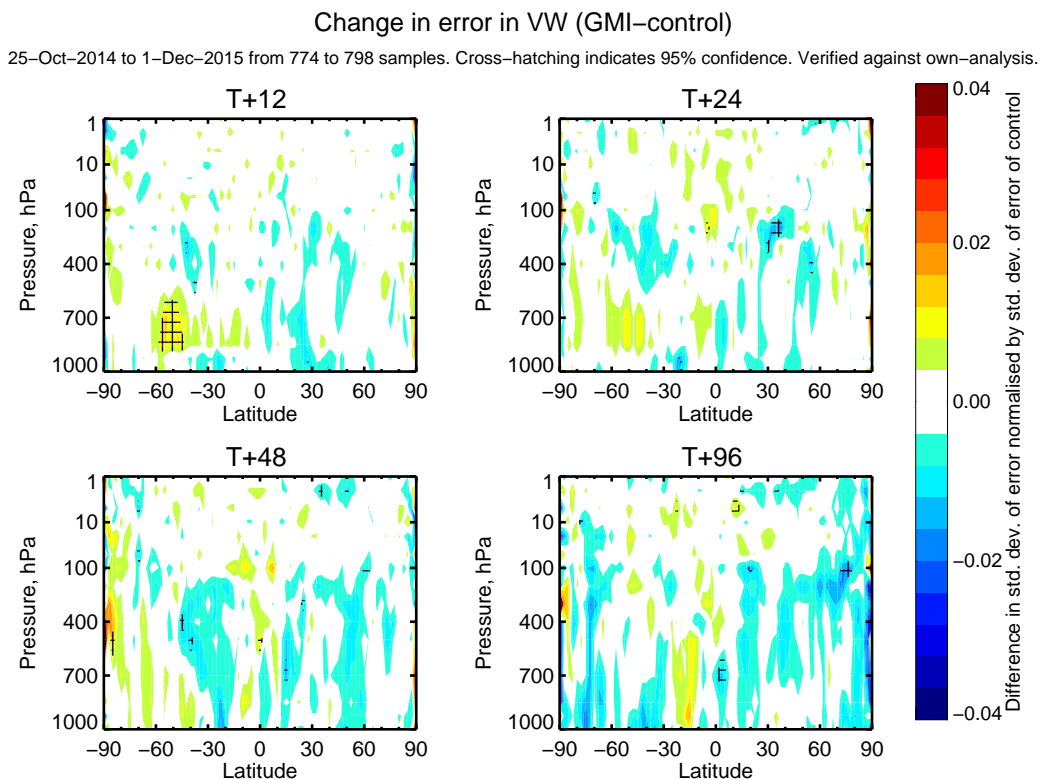
T+12

T+24

T+48

T+96

Figure 12: Normalised change in standard deviation of vector wind errors, as a function of latitude and pressure,
GMI on minus GMI off. Blue areas indicate wind errors are smaller in the experiment (GMI on) than the control.

Change in error in R (GMI – control)

25–Oct–2014 to 1–Dec–2015 from 774 to 798 samples. Verified against own–analysis.
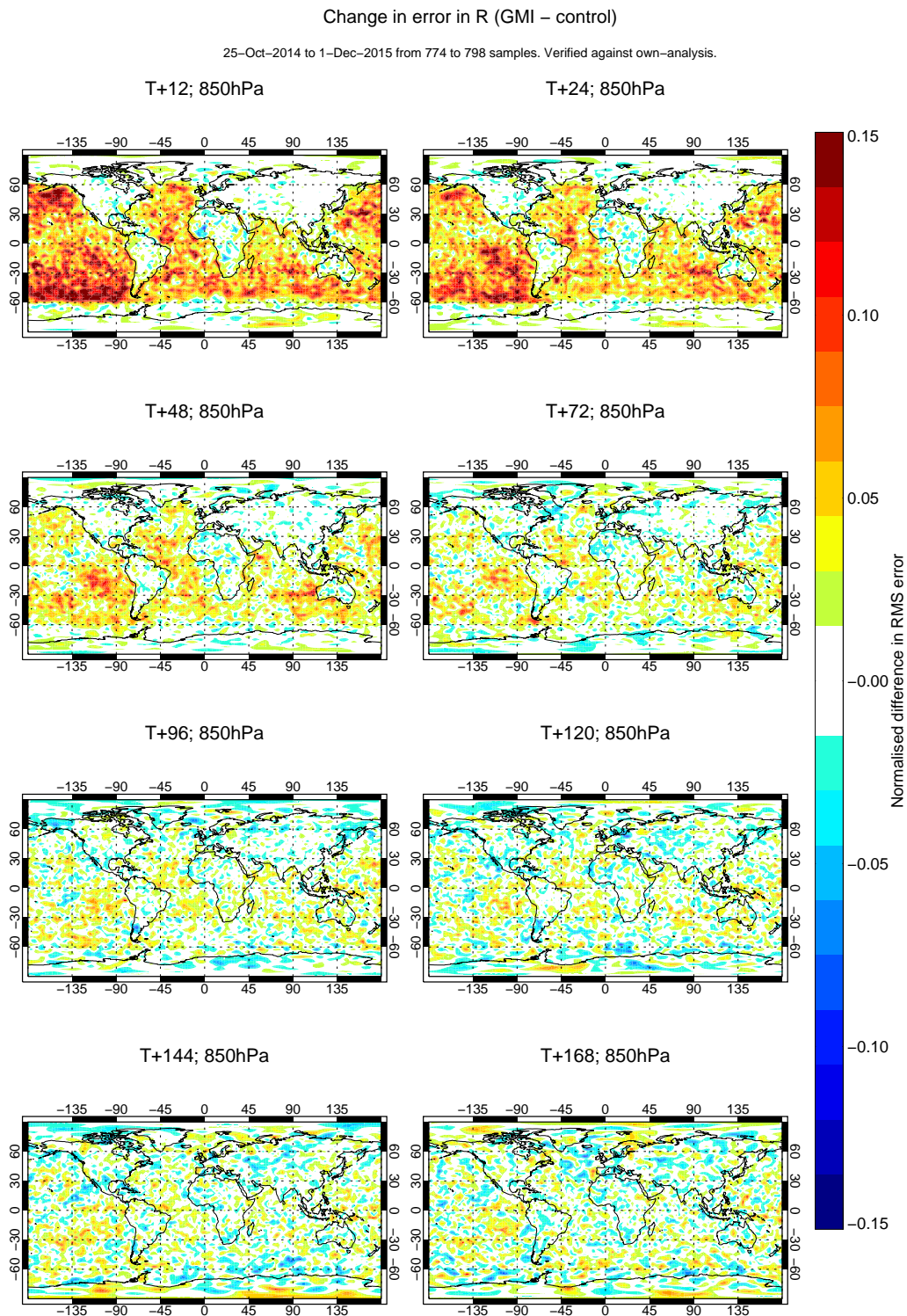

Figure 13: Normalised change in RMS error of relative humidity at 850 hPa, GMI on minus GMI off. Red areas indicate an increase in RMS error compared to the control (see text).
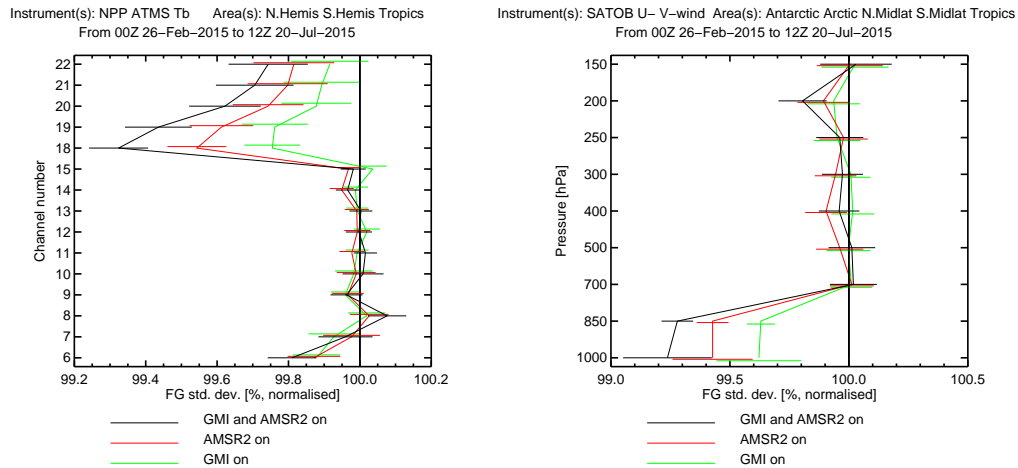
Figure 14: Comparing the impact of GMI and AMSR2: normalised change in standard deviation of FG departures of ATMS (brightness temperatures with water vapour and temperature sensitivity) and SATOB (winds)

Figure 13 maps the change in RMS error in relative humidity at 850 hPa. There are large apparent increases in RMS error, but this is again just an increase in the size of humidity increments, as has been well-established (e.g. Geer and Bauer, 2010; Kazumori et al., 2016; Geer et al., 2017). The fact that the apparent increases stay in the same place through the forecast range, and that they do not move with the flow (for example the land areas are completely unaffected) is consistent with the RMS error measuring a change in the analysis, rather than in the forecast. Also the observation fits show clear improvements in lower-tropospheric moisture from GMI assimilation. The own-analysis increment effect does however provide a map of where the GMI data are being assimilated: equatorwards of 60° and over oceans only.

3.3   Comparison to AMSR2

Given that AMSR2 was activated operationally at the same time as GMI, we tested both instruments in parallel on top of the SSMIS baseline, as well as both instruments together (the final operational configuration). This testing is available for a shorter period (26th Feb to 20th July 2016). Kazumori et al. (2016) give more details of the capabilities of AMSR2 and its assimilation. Both GMI and AMSR2 are assimilated over oceans only, with a latitude cutoff at 60°, and very similar screening and observation error modelling. The main differences are in the orbit (AMSR2 is a sun-synchronous polar orbiter); the channel availability (we assimilate one additional channel from AMSR2, a horizontally polarised 24 GHz channel, 24h, which perhaps gives more weight to total column water vapour information) and finally the swath width (931 km on GMI; 1450 km on AMSR2).

Fig. 14 summarises the results of the combined testing alongside AMSR2. Generally the impact of GMI is around 60% to 65% of that provided by AMSR2, but the assimilation of both instruments together gives greater benefit than assimilating either on their own. Forecast sensitivity to observation impact (FSOI) results from the operational system show impact from GMI that is around 80% that of AMSR2 (see Geer et al., 2017). The explanation is likely down to coverage. Although GMI provides more coverage at around 45° to 60° latitude due to its inclined orbit, this is probably more than counterbalanced by its narrower swath, which provides less coverage in the tropics than AMSR2 (around 60%). As explained earlier, this narrower swath comes because of GPM's lower altitude, which is necessary to achieve high-resolution, low-noise precipitation observations from DPR.

4 Results: high-frequency channels

4.1 Details

GMI's high frequency channels were finally available for assimilation trials once the ability to model multiple zenith angles had been added to the IFS, and a channel rotation bug (Sec. 2.2.3) had been corrected in our preprocessing. Assimilation of GMI humidity sounding channels (channels 12 and 13) is intended to become operational with IFS cycle 43r3 in mid 2017. This section examines the pre-merge testing in support of that change, but also includes testing of active assimilation of the 166 GHz channels (channels 10 and 11) that is not intended for operational assimilation. These channels are sensitive to a combination of lower-tropospheric moisture, cloud water and frozen hydrometeors. These sensitivities are hard to separate, and in some cases they have contradictory effects: for example an increase in cloud water generally increases brightness temperatures; an increase in frozen hydrometeors generally decreases them. It is up to the assimilation system to make correct use of the information, but it may be challenging. However, other GMI channels offer cleaner sensitivities to water vapour (e.g. 22v) cloud water (e.g. 37v) and frozen hydrometeors (e.g 183 GHz). Hence, use of all the GMI channels together should constrain these sensitivities and could allow them to be used without problem.

However, the humidity sounding channels (e.g. 183 GHz) cannot be expected to show large impacts. ECMWF already uses 9 other microwave humidity sounding instruments, most of them in all-sky conditions, along with many infrared instruments with similar capabilities (Geer et al., 2017). It would be hard for any new sensor to show a big impact in such a well-observed system. Also, GMI only offers 2 channels at 183 GHz sensing the middle- rather than upper-troposphere; the existing microwave sensors all offer at least 3 channels that span middle- and upper-troposphere. However, beneficial impact under these conditions would indicate that the benefit from adding more water vapour sounding radiances has not yet saturated.

Experiments are based on the combined winter and summer pre-43r3 testing, using as a control cycle 43r1 with horizontal resolution of TCo399. The winter testing covers 5th November 2015 to 28th February 2016, and the summer testing 5th May to 31st August 2016, giving a combined total of around 8 months. Two experiments have been performed: adding the two 183 GHz channels (the contribution for 43r3) and adding all four high frequency channels (183 GHz plus 166v and 166h).

4.2 Results

Figures 15, 16 and 17 show the same set of FG departure statistics used in the previous section, to examine the impact of assimilating GMI high-frequency channels on short range forecasts. Figure 18 shows the impact on midlatitude medium-range scores.

We first consider the impact of the GMI 183 GHz channels on their own. The red lines on Figs. 15, 16 and 17 show there are small beneficial impacts in humidity and temperature fits, but no sign of an impact on winds. Fits to the mid-troposphere humidity channels of ATMS (channels 18 to 20) are improved by around 0.1% and there are also improvements of similar size to IASI mid- and upper-troposphere channels (around channel number 3110). There are also improvements in fit to AMSU-A channels 5 and 9. However, there is no sign of impact on midlatitude forecast scores (Figs. 18 and 19). The combined medium-range forecast impact of the existing 7 microwave imagers and sounders is around 4%. Since the forecast impact of new instruments does not add linearly, but instead instead behaves in a way analogous to the $1/\sqrt{n}$ behaviour of the standard error (see e.g. Bauer et al., 2014), we would
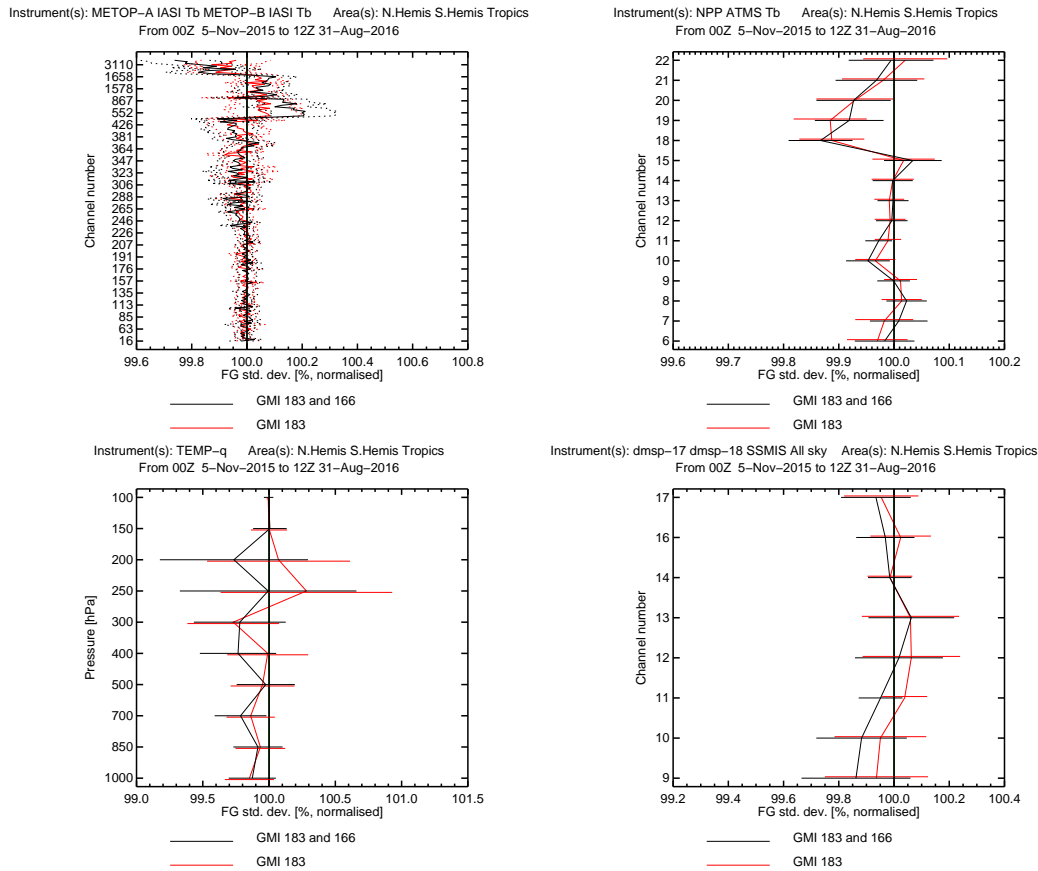
Figure 15: Normalised change in standard deviation of FG departures for observations with humidity sensitivity (and also temperature sensitivity; as a percentage of experiment divided by control): top left, IASI; top right, ATMS; bottom left, radiosonde TEMP-q; bottom right SSMIS

be expecting an impact less than 0.5%. Even this maximum estimated impact would be too small to identify as a significant result, given the size of the 95% confidence range in these figures. The amount of testing required to identify any impact from GMI on medium-range scores in the context of the full observing system would be unfeasibly large (see Geer, 2016). In summary, the impact on humidity and temperature observation fits are a sign that GMI 183 GHz channels are bringing new information in the context of an already very well-observed system, and we would expect some forecast benefit through the same mechanisms behind the successful assimilation of microwave humidity sounders that are already in the system (Geer, 2013; Geer et al., 2014, 2017). However, it would not be practical to confirm this by experiment.

The combination of the 183 GHz channels with the 166 GHz channels has a larger impact on temperature and wind fits to observations. The temperature fits are not significantly affected except AMSU-A channel 5, which is improved. There are also some beneficial wind impacts, at least against SATOBs (AMVs) at 850 hPa. However, there are apparently worse fits at 700 hPa to conventional wind observations ('WIND2'), though these are localised to the NH. There is no sign of the wind or other dynamical forecasts deteriorating in the analysis-based forecast scores. The observation fits do also show deteriorations with respect to IASI in a channel range from 500 to 900, which are lower-tropospheric sounding channels. However, these are not seen in any other infrared instruments (i.e. they are not seen in CrIS, AIRS or HIRS fits). On balance, however, the impact on wind and temperature is slightly beneficial.

Instrument(s): TEMP–T   Area(s): N.Hemis S.Hemis Tropics
From 00Z 5–Nov–2015 to 12Z 31–Aug–2016

Instrument(s): AQUA metop–a metop–b noaa–15 noaa–18 noaa–19 sky – AMSU–A
Area(s): N.Hemis S.Hemis Tropics
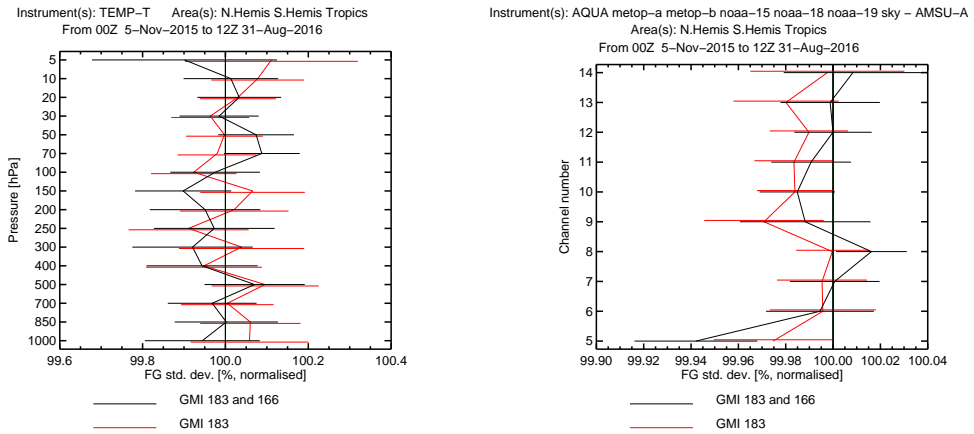From 00Z 5–Nov–2015 to 12Z 31–Aug–2016

Figure 16: Normalised change in standard deviation of FG departures for temperature-related observations (as a percentage of experiment divided by control): left, radiosonde (TEMP-T); right, AMSU-A

Instrument(s): AIREP AMprofiler EUprofiler JPprofiler PILOT TEMP – Uwind Vwind
Area(s): Europe Japan N.Amer N.Hemis S.Hemis Tropics
From 00Z 5–Nov–2015 to 12Z 31–Aug–2016

Instrument(s): SATOB U– V–wind Area(s): Antarctic Arctic N.Midlat S.Midlat Tropics
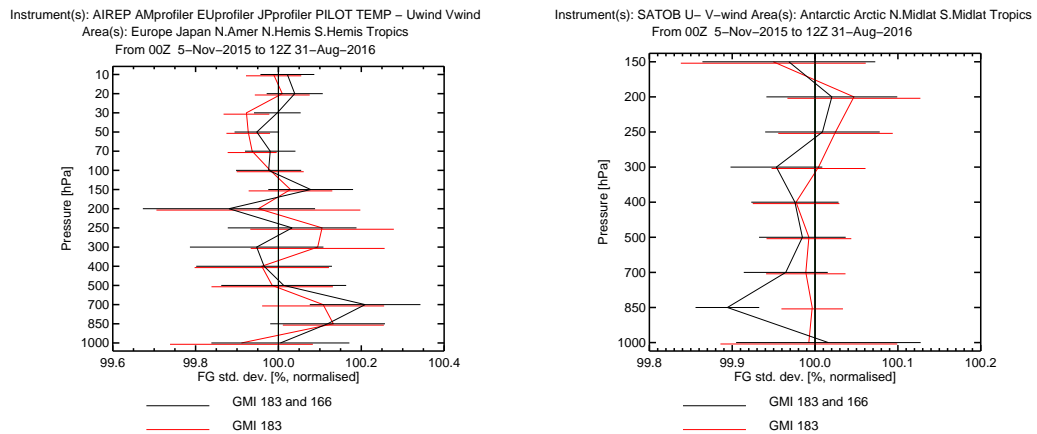From 00Z 5–Nov–2015 to 12Z 31–Aug–2016

Figure 17: Normalised change in standard deviation of FG departures for wind observations (as a percentage of experiment divided by control): left, all conventional winds (WIND2); right, atmospheric motion vectors (SATOB)
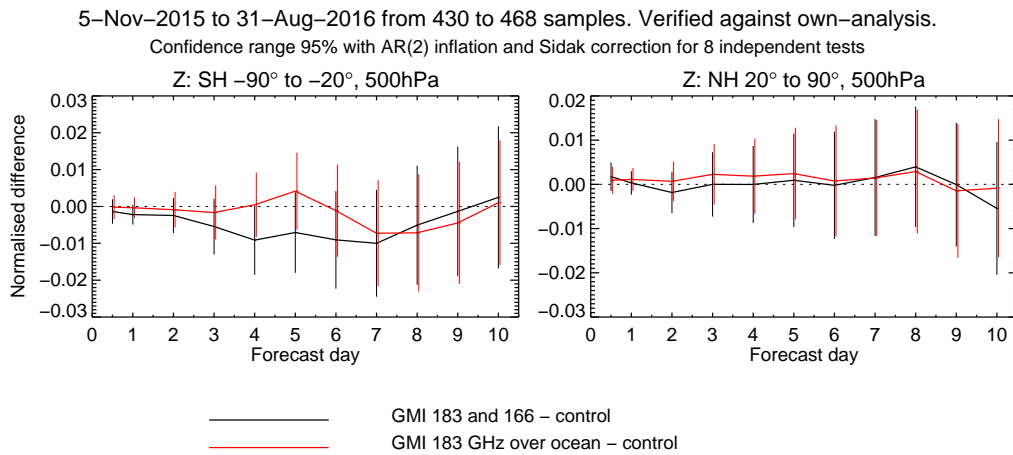
5–Nov–2015 to 31–Aug–2016 from 430 to 468 samples. Verified against own–analysis.
Confidence range 95% with AR(2) inflation and Sidak correction for 8 independent tests

GMI 183 and 166 – control
GMI 183 GHz over ocean – control

Figure 18: Normalised change in RMS error in 500 hPa geopotential.

Change in error in VW (GMI 183 GHz over ocean–control)
5–Nov–2015 to 31–Aug–2016 from 430 to 468 samples. Cross–hatching indicates 95% confidence. Verified against own–analysis.
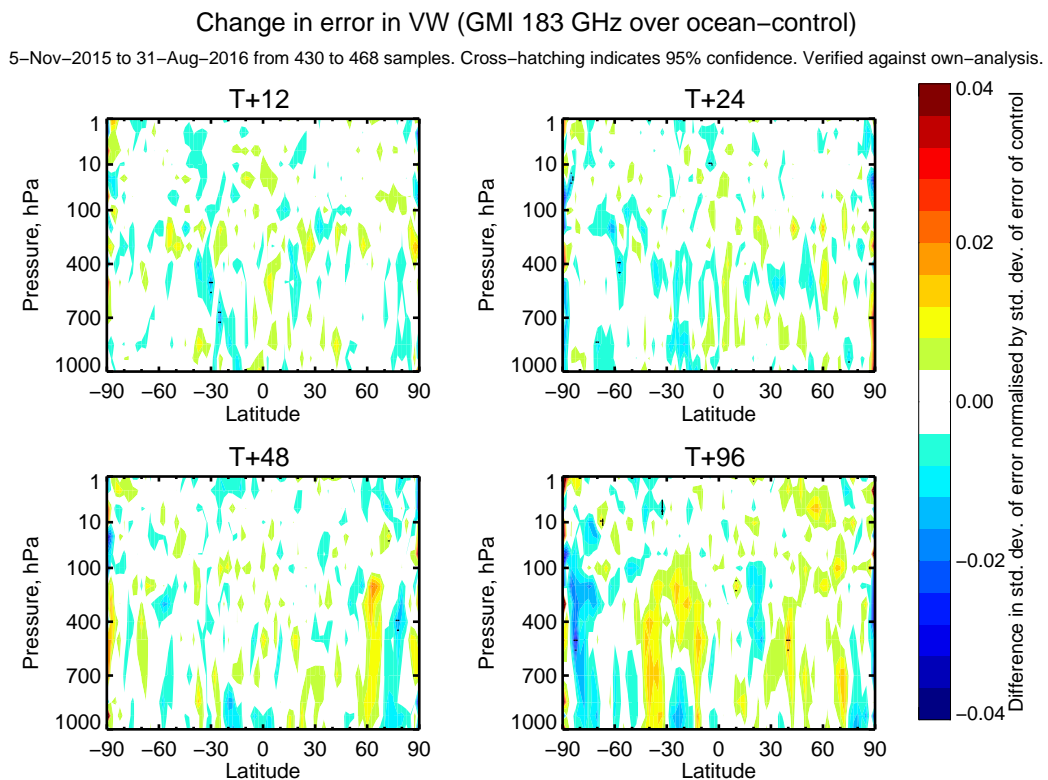

Figure 19: Normalised change in standard deviation of vector wind errors: GMI with 183 GHz assimilation minus control (183 GHz + 166 GHz experiment not shown).
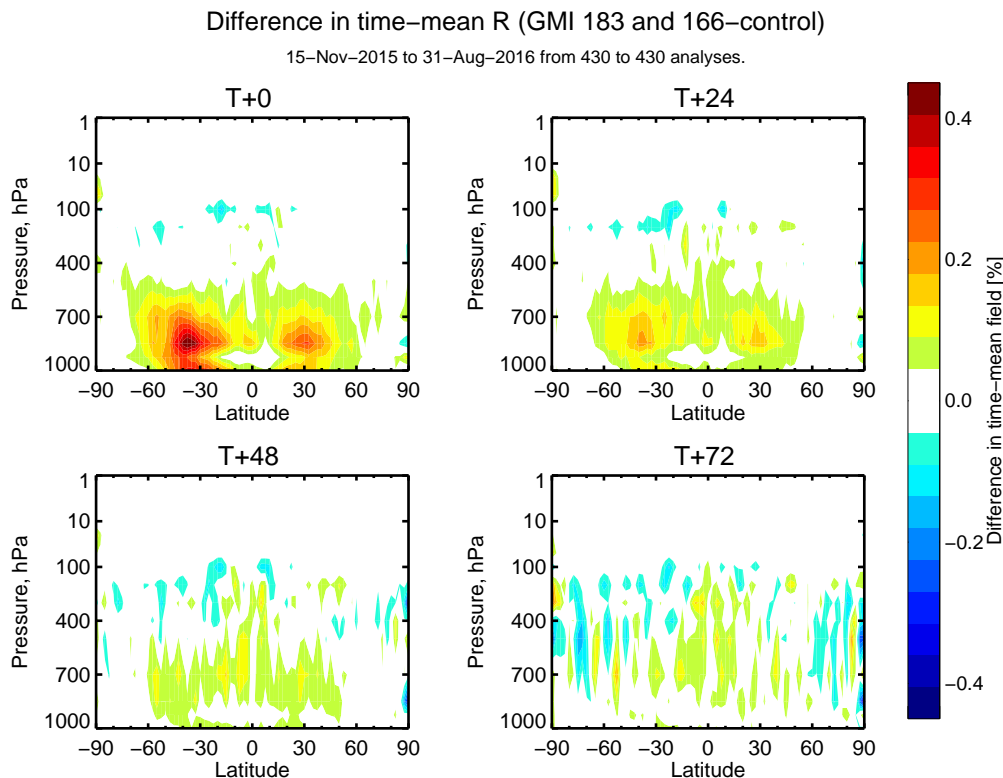
Figure 20: Mean change in relative humidity (R) between GMI with 183 GHz + 166 GHz assimilation and control

Although the humidity fits in Fig. 15 show little change with the assimilation of 166 GHz alongside 183 GHz channels of GMI, adding 166 GHz does cause an increase in relative humidity of 0.1% to 0.3% in the analysis and short range forecast (Fig. 20). This is predominantly in the subtropics in regions of stratocumulus or possibly of transition to trade-cumulus. In these regions, modelled cloud water amounts are too low, and the diurnal cycle is insufficiently strong, leading to noticeable positive biases in microwave imager FG departures (Kazumori et al., 2016). These biases are not corrected by VarBC but despite this their assimilation is beneficial (Lonitz and Geer, 2017). The 166 GHz channels are also sensitive to this model bias, and it is likely that the analysis is creating more relative humidity in order to generate more liquid water cloud in these areas, so better matching the observations. The moistening of the lower troposphere brings the analysis and forecast mean state a little closer to the radiosondes (Fig. 22) and reduces the bias relative to GPSRO from +0.03 to +0.02 (in units of normalised bending angle) at 3 km altitude (not shown; GPSRO is sensitive to humidity in the lower troposphere). This moistening also counteracts the tendency of microwave imager assimilation to dry the analysis around the 850 hPa level, and thus it may be genuinely beneficial to the accuracy of humidity in the analysis.

Short-range forecast errors in relative humidity and temperature also seem to improve at low levels, particularly in the tropics and subtropics, and with significant impacts sustained out to at least 48 h (Figs. 23 and 24). However, the interpretation of own-analysis forecast scores at short ranges in the tropics is extremely tricky. These changes are likely nothing more than a reduction in size of the tropical increments in R and T. However, the reduction is present in the equivalents of these figures based on standard deviation (not shown) so it is more than just an effect of mean changes in the analysis. These results are promising and it would be worth doing more investigation into the assimilation of the 150 GHz – 166 GHz window channels, which are available on many satellites.
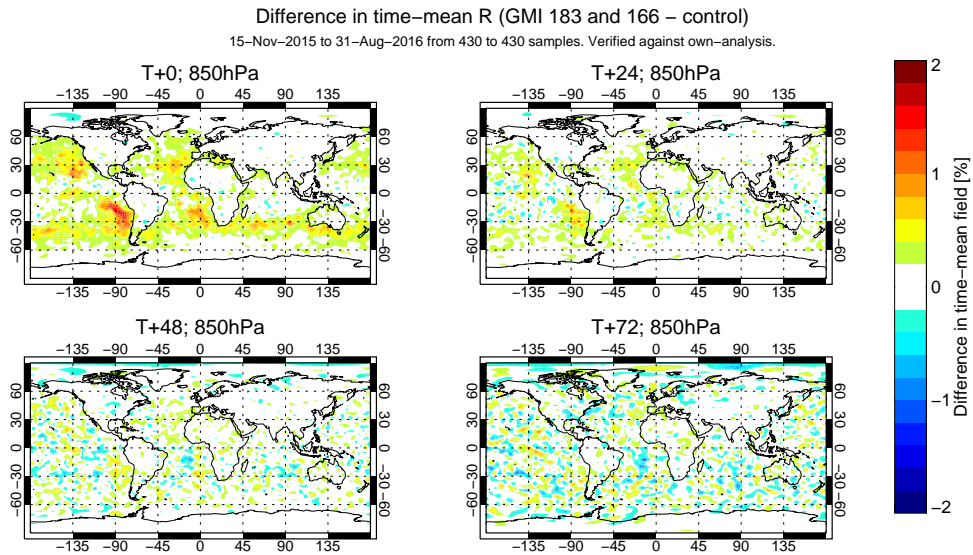
Figure 21: Mean change in relative humidity (R) between GMI with 183 GHz + 166 GHz assimilation and control at 850 hPa
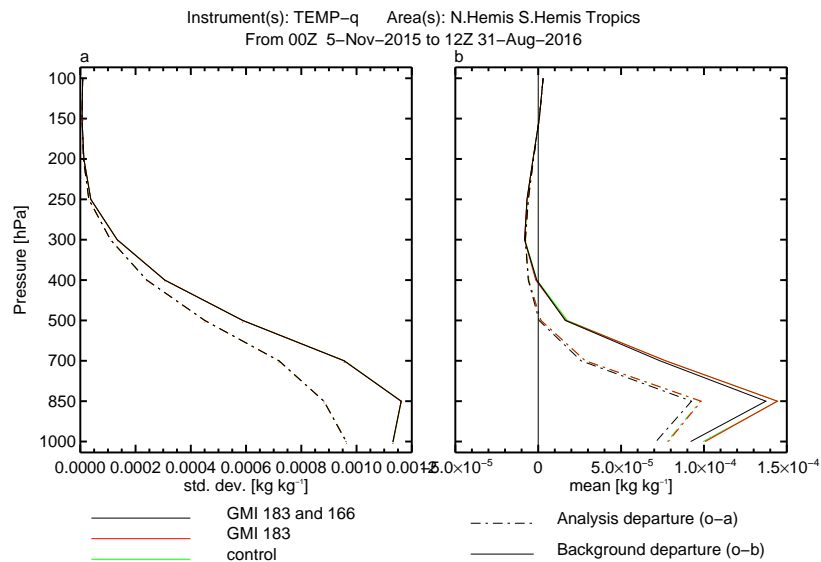

Figure 22: Traditional obstat for radiosonde humidity (TEMP-q): a) Standard deviation of FG and analysis fit; b) Mean FG and analysis departure bias

Change in error in R (GMI 183 and 166−control)

5−Nov−2015 to 31−Aug−2016 from 430 to 468 samples. Cross−hatching indicates 95% confidence. Verified against own−analysis.
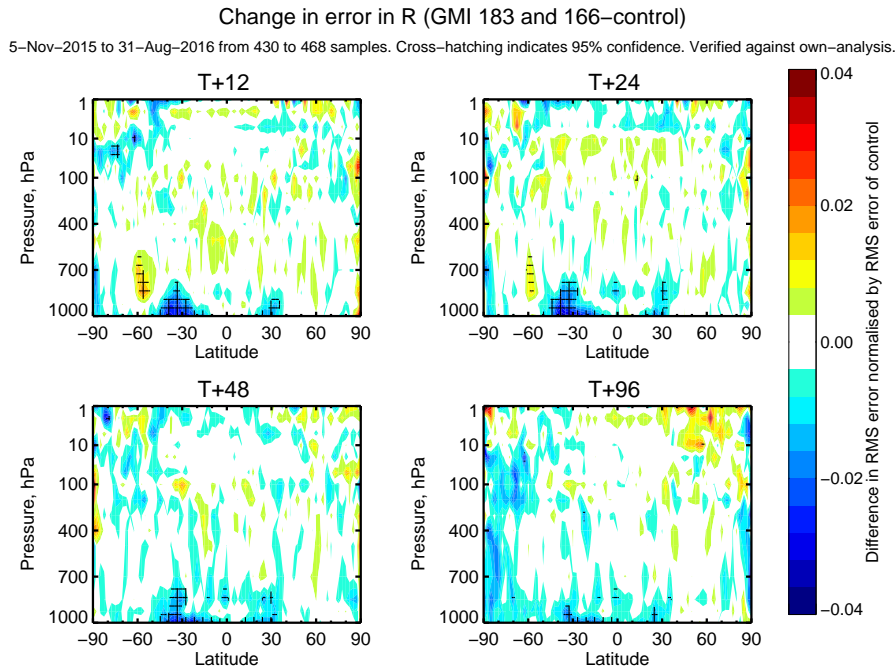

Figure 23: Normalised change in RMS of relative humidity errors: GMI with 183 GHz + 166 GHz assimilation minus control (183 GHz experiment not shown).
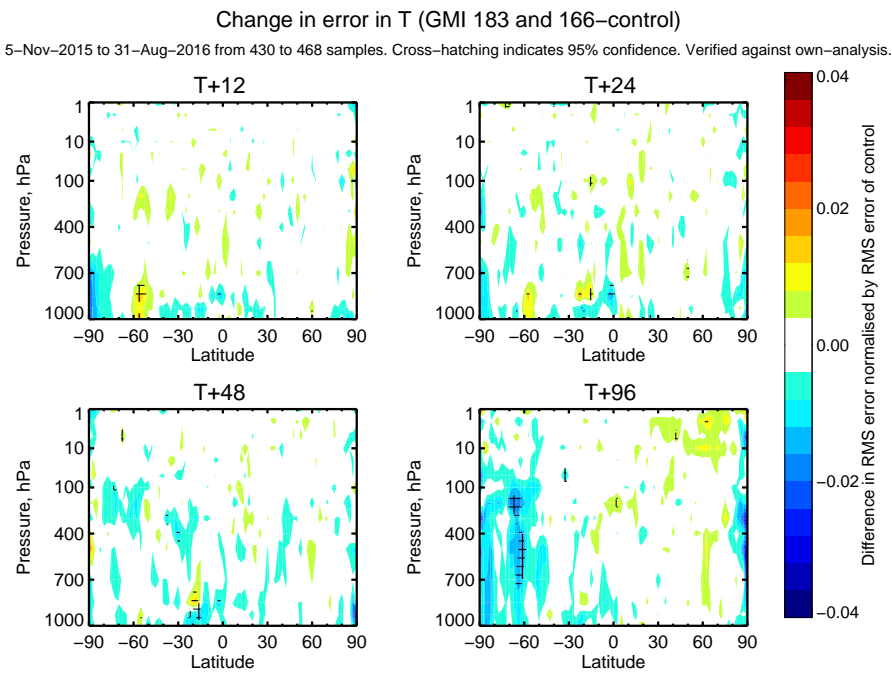
Change in error in T (GMI 183 and 166−control)

5−Nov−2015 to 31−Aug−2016 from 430 to 468 samples. Cross−hatching indicates 95% confidence. Verified against own−analysis.

Figure 24: Normalised change in RMS of temperature errors: GMI with 183 GHz + 166 GHz assimilation minus control (183 GHz experiment not shown).

5 Conclusion

GMI is a well-calibrated microwave imager, with modifications compared to previous imagers that should eliminate all of the known issues with this type of instrument. Biases between GMI observations and ECMWF simulations are all within the expected calibration uncertainty of 0.8 K, except in the 89 GHz channels where model errors could be to blame. If the estimated calibration uncertainty of GMI is correct, this suggests that the ECMWF simulated brightness temperatures are also well-calibrated, at least under clear-sky conditions. However, the good agreement could also have arisen by chance and another well-calibrated sensor, AMSR-2, shows larger biases compared to ECMWF simulations. Resolving these questions of absolute calibration is an aim of the ongoing GAIA-CLIM project (see e.g. Lawrence et al., 2017).

Activating GMI's microwave imaging channels (from 19 GHz to 90 GHz) is clearly beneficial; they have been assimilated operationally since 12th August 2015. This memo documents GMI's implementation in the ECMWF system, and it takes advantage of a long testing period to gain a clear picture of its impact (13 months of scores were available). The impact was measured on top of the full operational observing system, but with the assimilation of microwave imager data only from SSMIS F-17 (in other words, AMSR2 and GMI were excluded from this control). The impact of GMI included around a 0.5% improvement in the quality of short-range humidity forecasts and also significant improvements in lower-tropospheric temperature and winds, which led to medium-range forecast improvements also of around 0.5%. These results are consistent with results from other microwave imagers (e.g. Kazumori et al., 2016; Geer et al., 2017).

These long experiments have also confirmed that microwave imager assimilation has a small negative impact on observation fits in the tropical stratosphere. This has been seen before, for example as a slight increase in the standard deviation of FG departures against channel 9 of AMSU-A, a lower stratospheric channel (Kazumori et al., 2016). For GMI, the main impact was on AMSU-A channels 10 and 11, which peak a little higher in the atmosphere. The degradations might be associated with the assimilation of convection, and the generation of gravity waves and tropical waves from this that are physically representative but not exactly matched to their real-world counterparts in terms of position or phase-speed. These waves can propagate into the stratosphere where they could impact observation fits. An alternative hypothesis could be background error correlations, possibly incorrect, between troposphere and stratosphere. The effect does not propagate into the medium-range forecasts, it is not visible in own-analysis verification, and it is very small compared to the clear benefits to tropospheric forecasts coming from all-sky microwave imager assimilation. Also, the stratospheric impact of all-sky microwave humidity sounders is actually quite beneficial, particularly in the tropics (Geer et al., 2014), possibly through a similar mechanism based on tropical waves, and so the overall impact of all-sky assimilation on the stratosphere is still beneficial (Geer et al., 2017). The main conclusion is simply to confirm that all-sky assimilation does influence the stratosphere, with a good chance this may be through the links between convection and tropical wave activity; this deserves further exploration.

GMI's high frequency channels (at 166 GHz to 183 GHz) have not been available for testing until recent technical and scientific upgrades at ECMWF. Activating the 183 GHz humidity sounding channels gives a 0.1% improvement in short-range fits to other humidity observations. The small size of this impact is likely explained by a number of factors. There are now 9 other microwave humidity sounding instruments being actively assimilated, most of them in all-sky conditions over almost all surface types (ocean, sea-ice, and land including snow-covered areas). There are also many infrared instruments with similar sensitivities. GMI has less coverage than other microwave sounders due to a necessarily narrower swath, and only two 183 GHz channels (compared to 3 or more on similar sounders); further, it has not yet been

implemented over land or sea-ice. Unsurprisingly, no impacts on dynamical forecasts have been seen, but even with 8 months of experimentation, any expected impact would be much smaller than the size of the 95% confidence range in the medium range. As there are no downsides to assimilating the data, and given the strong positive benefits of adding previous microwave humidity sounding observations (Geer et al., 2017) it is recommended for operational implementation with cycle 43r3 in mid 2017.

GMI's 166 GHz channels are microwave imaging channels with strong sensitivity to water vapour, liquid water cloud and frozen hydrometeors. Similar channels exist on SSMIS and MHS, but none have been tested for assimilation before, so an experiment was made for GMI. The effect is to moisten the subtropical atmosphere in regions of maritime stratocumulus (or transition to trade cumulus) where the forecast model produces insufficient liquid water cloud. This also reduces the analysis and short-range forecast dry bias against radiosonde humidities and GPSRO in the lower troposphere. Further, it reduces the size of tropical wind and temperature increments and short-range forecast errors, not just in terms of means but also of standard deviations. In observation fits, there are mixed signals, but most promising is a small beneficial impact on AMSU-A channel 5, which may suggest a real improvement in lower tropospheric temperature forecasts. It would also be possible to assimilate the 150 GHz channel of SSMIS on DMSP-F17, which has similar properties to the 166 GHz channels, but possibly not the equivalents on MHS since those channels are used to determine the observation error. The impact is sufficiently promising that it should be investigated further, ideally by testing with both SSMIS and GMI simultaneously, to get a stronger signal.

Acknowledgements

References

Bauer, P., A. J. Geer, P. Lopez, and D. Salmond (2010). Direct 4D-Var assimilation of all-sky radiances: Part I. Implementation. *Quart. J. Roy. Meteorol. Soc. 136*, 1868–1885.

Bauer, P., P. Lopez, D. Salmond, and A. J. Geer (2006). Assimilation of cloud and precipitation affected microwave radiances. *ECMWF Tech. Memo., 502, available from http://www.ecmwf.int*.

Bauer, P., G. Radnóti, S. Healy, and C. Cardinali (2014). Gnss radio occultation constellation observing system experiments. *Monthly Weather Review 142*(2), 555–572.

Bell, W., B. Candy, N. Atkinson, F. Hilton, N. Baker, N. Bormann, G. Kelly, M. Kazumori, W. Campbell, and S. Swadley (2008). The assimilation of SSMIS radiances in numerical weather prediction models. *IEEE Trans. Geosci. Remote Sensing 46*, 884–900.

Berg, W., S. Bilanow, R. Chen, S. Datta, D. Draper, H. Ebrahimi, S. Farrar, W. L. Jones, R. Kroodsma, D. McKague, V. Payne, J. Wang, T. Wilhiet, and J. X. Yang (2016). Intercalibration of the GPM microwave radiometer constellation. *Journal of Atmospheric and Oceanic Technology 33*(12), 2639–2654.

Bormann, N., A. Geer, and S. English (2012). Evaluation of the microwave ocean surface emissivity model FASTEM-5 in the IFS. *ECMWF Technical Memorandum 667*.

Dee, D. (2004). Variational bias correction of radiance data in the ECMWF system. In *ECMWF workshop proceedings: Assimilation of high spectral resolution sounders in NWP, 28 June – 1 July, 2004*, pp. 97–112. Eur. Cent. for Med. Range Weather Forecasts, Reading, UK, available from http://www.ecmwf.int.

Draper, D. W., D. A. Newell, F. J. Wentz, S. Krimchansky, and G. M. Skofronick-Jackson (2015). The global precipitation measurement (GPM) microwave imager (GMI): Instrument overview and early on-orbit performance. *IEEE J. Sel. Top. App. Earth Obs. Rem. Sens. 8*(7), 3452–3462.

Geer, A. J. (2013). All-sky assimilation: better snow-scattering radiative transfer and addition of SSMIS humidity sounding channels. *ECMWF Tech. Memo., 706, available from http://www.ecmwf.int*.

Geer, A. J. (2016). Significance of changes in forecast scores. *Tellus A 68*, 30229, http://dx.doi.org/10.3402/tellusa.v68.30229.

Geer, A. J., F. Baordo, K. Befort, N. Bormann, S. English, M. Kazumori, H. Lawrence, P. Lean, and C. Lupu (2017). The growing impact of satellite observations sensitive to humidity, cloud and precipitation. *Quart. J. Roy. Meteorol. Soc.*, in preparation.

Geer, A. J., F. Baordo, N. Bormann, and S. English (2014). All-sky assimilation of microwave humidity sounders. *ECMWF Tech. Memo., 741, available from http://www.ecmwf.int*.

Geer, A. J. and P. Bauer (2010). Enhanced use of all-sky microwave observations sensitive to water vapour, cloud and precipitation. *Published simultaneously as ECMWF Technical Memoranda 620 and ECMWF/EUMETSAT fellowship reports 20*.

Geer, A. J. and P. Bauer (2011). Observation errors in all-sky data assimilation. *Quart. J. Roy. Meteorol. Soc. 137*, 2024–2037.

Geer, A. J., P. Bauer, and N. Bormann (2010). Solar biases in microwave imager observations assimilated at ECMWF. *IEEE Trans. Geosci. Remote Sens. 48*, 2660 – 2669.

Gong, J. and D. L. Wu (2017). Microphysical properties of frozen particles inferred from global precipitation measurement (GPM) microwave imager (GMI) polarimetric measurements. *Atmos. Chem. Phys. Discuss.*, In review.

Järvinen, H. and P. Unden (1997). Observation screening and background quality control in the ECMWF 3D-Var data assimilation system. *ECMWF Tech. Memo., 236, available from http://www.ecmwf.int*.

Kazumori, M. and S. J. English (2015). Use of the ocean surface wind direction signal in microwave radiance assimilation. *Quarterly Journal of the Royal Meteorological Society 141*(689), 1354–1375.

Kazumori, M., A. J. Geer, and S. J. English (2016). Effects of all-sky assimilation of GCOM-W/AMSR2 radiances in the ECMWF numerical weather prediction system. *Quart. J. Roy. Meteorol. Soc. 142*, 721–737.

Kummerow, C., J. Simpson, O. Thiele, W. Barnes, A. Chang, E. Stocker, R. Adler, A. Hou, R. Kakar, F. Wentz, P. Ashcroft, T. Kozu, Y. Hong, K. Okamoto, T. Iguchi, H. Kuroiwa, E. Im, Z. Haddad, G. Huffman, B. Ferrier, W. S. Olson, E. Zipser, E. A. Smith, T. T. Wilheit, G. North, T. Krishnamurti, and K. Nakamura (1998). The status of the Tropical Rainfall Measuring Mission (TRMM) after two years in orbit. *J. App. Met. 39*, 1965–1982.

Lawrence, H., F. Carminati, W. Bell, N. Bormann, S. Newman, N. Atkinson, A. Geer, S. Migliorini, Q. Lu, and K. Chen (2017). An evaluation of FY-3C MWRI and assessment of the long-term quality of FY-3C MWHS-2 at ECMWF and the Met Office. *ECMWF Tech. Memo. 798.*

Lonitz, K. and A. Geer (2017). Effect of assimilating microwave imager observations in the presence of a model bias in marine stratocumulus. *EUMETSAT/ECMWF Fellowship Programme Research Report, 44, available from http://www.ecmwf.int.*

Meunier, L.-F., S. English, and P. Janssen (2014). Improved ocean emissivity modelling for assimilation of microwave imagers using foam coverage derived from a wave model. *NWP-SAF visiting scientist report NWPSAF-EC-VS-024, available from https://nwpsaf.eu/.*

Wentz, F., P. Ashcroft, and C. Gentemann (2001). Post-launch calibration of the TRMM Microwave Imager. *IEEE Trans. Geosci. Remote Sensing 39*, 415–422.